Homogeneity assessment of the SuperCam calibration targets onboard rover perseverance

J.M. Madariaga, J. Aramendia, G. Arana, K. Castro, L. Gómez-Nubla, S. Fdez-Ortiz de Vallejuelo, C. Garcia-Florentino, M. Maguregui, J.A. Manrique, G. Lopez-Reyes, et al.

J.M. Madariaga, J. Aramendia, G. Arana, K. Castro, L. Gómez-Nubla, et al.. Homogeneity assessment of the SuperCam calibration targets onboard rover perseverance. Analytica Chimica Acta, 2022, 1209, pp.339837. 10.1016/j.aca.2022.339837 . hal-03840635

HAL Id: hal-03840635
https://hal.science/hal-03840635v1

Analytica Chimica Acta 1209 (2022) 339837

Contents lists available at ScienceDirect

Analytica Chimica Acta

journal homepage: www.elsevier.com/locate/aca

Homogeneity assessment of the SuperCam calibration targets onboard rover perseverance

J.M. Madariaga [a,*], J. Aramendia [a], G. Arana [a], K. Castro [a], L. Gómez-Nubla [a], S. Fdez-Ortiz de Vallejuelo [a], C. Garcia-Florentino [a], M. Maguregui [a], J.A. Manrique [b], G. Lopez-Reyes [b], J. Moros [c], A. Cousin [d], S. Maurice [d], A.M. Ollila [e], R.C. Wiens [e,f], F. Rull [b], J. Laserna [c], V. Garcia-Baonza [g,l], M.B. Madsen [h], O. Forni [d], J. Lasue [d], S.M. Clegg [e], S. Robinson [e], P. Bernardi [i], A.J. Brown [j], P. Caïs [k], J. Martinez-Frias [l], P. Beck [m], S. Bernard [n], M.H. Bernt [d], O. Beyssac [n], E. Cloutis [o], C. Drouet [p], G. Dromart [q], B. Dubois [d], C. Fabre [r], O. Gasnault [d], I. Gontijo [s], J.R. Johnson [t], J. Medina [b], P.-Y. Meslin [d], G. Montagnac [q], V. Sautter [n], S.K. Sharma [u], M. Veneranda [b], P.A. Willis [s]

[a] Dept. of Analytical Chemistry, University of the Basque Country (UPV/EHU), 48940, Leioa, Spain
[b] Unidad Asociada UVA-CSIC-CAB, University of Valladolid (UVA), Valladolid, Spain
[c] Dept. of Analytical Chemistry, University of Malaga (UMA), Malaga, Spain
[d] Institut de Recherche en Astrophysique et Planetologie (IRAP), CNRS, UMR, 5277, Toulouse, France
[e] Los Alamos National Laboratory (LANL), Los Alamos, NM, USA
[f] Earth, Atmospheric, and Planetary Sciences, Purdue University, West Lafayette, IN, USA
[g] University Complutense of Madrid (UCM), Madrid, Spain
[h] Niels Bohr Institute, University of Copenhagen, Copenhagen, Denmark
[i] Laboratoire d'Etudes Spatiales et d'Instrumentation en Astrophysique, Meudon, France
[j] NASA HQ, Severna Park, MD, USA
[k] Laboratoire d'astrophysique de Bordeaux, Univ. Bordeaux, CNRS, France
[l] Institute of Geosciences IGEO (CSIC-UCM), Madrid, Spain
[m] Institute de Planetologie et d'Astrophysique de Grenobel, Université Grenoble Alpes, Grenoble, France
[n] IMPMC, Museum National d'Histoire Naturelle, CNRS, Sorbonne Université, Paris, France
[o] Dept. of Geography, University of Winnipeg, 515 Portage Avenue, Winnipeg, MN, R3B 2E9, Canada
[p] Centre Interuniversitaire de Recherche et d'Ingénierie des Matériaux (CIRIMAT), CNRS, Toulouse, France
[q] Laboratoire de Géologie de Lyon, Lyon, France
[r] GeoRessources Vandoeuvre les Nancy, Nancy, France
[s] Jet Propulsion Laboratory, Pasadena, USA
[t] Applied Physics Laboratory, Johns Hopkins University, Laurel, MD, 20723-6005, USA
[u] University of Hawaii, Manoa, HI, USA

ARTICLE INFO

Keywords:
Mars2020
Perseverance rover
SuperCam calibration target
Elemental homogeneity
Mineral homogeneity
Uncertainties

ABSTRACT

The SuperCam instrument, onboard the Perseverance rover (Mars 2020 mission) is designed to perform remote analysis on the Martian surface employing several spectroscopic techniques such as Laser Induced Breakdown Spectroscopy (LIBS), Time-Resolved Raman (TRR), Time-Resolved Fluorescence (TRF) and Visible and Infrared (VISIR) reflectance. In addition, SuperCam also acquires high-resolution images using a color remote micro-imager (RMI) as well as sounds with its microphone. SuperCam has three main subsystems, the Mast Unit (MU) where the laser for chemical analysis and collection optics are housed, the Body Unit (BU) where the different spectrometers are located inside the rover, and the SuperCam Calibration Target (SCCT) located on the rover's deck to facilitate calibration tests at similar ambient conditions as the analyzed samples. To perform adequate calibrations on Mars, the 22 mineral samples included in the complex SCCT assembly must have a very homogeneous distribution of major and minor elements. The analysis and verification of such homogeneity for the 5–6 replicates of the samples included in the SCCT has been the aim of this work. To verify the physic-

---

* Corresponding author.
E-mail address: juanmanuel.madariaga@ehu.es (J.M. Madariaga).

https://doi.org/10.1016/j.aca.2022.339837
Received 18 January 2022; Received in revised form 17 March 2022; Accepted 13 April 2022

chemical homogeneity of the calibration targets, micro Energy Dispersive X-ray Fluorescence (EDXRF) imaging was first used on the whole surface of the targets, then the relative abundances of the detected elements were computed on 20 randomly distributed areas of 100 × 100 μm. For those targets showing a positive Raman response, micro-Raman spectroscopy imaging was performed on the whole surface of the targets at a resolution of 100 × 100 μm. The %RSD values (percent of relative standard deviation of mean values) for the major elements measured with EDXRF were compared with similar values obtained by two independent LIBS set-ups at spot sizes of 300 μm in diameter. The statistical analysis showed which elements were homogeneously distributed in the 22 mineral targets of the SCCT, providing their uncertainty values for further calibration. Moreover, nine of the 22 targets showed a good Raman response and their mineral distributions were also studied. Those targets can be also used for calibration purposes of the Raman part of SuperCam using the wavenumbers of their main Raman bands proposed in this work.

1. Introduction

The Mars 2020 Perseverance rover is the current NASA flagship mission to Mars and the first step in an international Mars sample return program [1], which landed in Jezero crater February 18, 2021 with the aim to fulfill four main objectives [1]. The geology and potential habitability will be studied, as well as the search for evidence of biomarkers or reservoirs where they could be preserved. Moreover, 43 carefully selected samples will be collected for the future Mars Sample Return Mission. Perseverance leverages the architecture of the Curiosity rover [2] and the heritage of part of the payload. However, the payload included in Perseverance covers different optical and spectroscopic instruments than the previous Curiosity rover in order to answer properly the ambitious objectives set for this Mars2020 mission.

One of the new instruments is SuperCam [3,4], derived from the heritage of ChemCam [5,6]. SuperCam is a standoff instrument, designed to be a multianalytical suite of several coaligned analytical techniques for remote sensing: Laser Induced Breakdown Spectroscopy (LIBS), Time-Resolved Raman and Luminescence (TRR/TRL), Visible and Infrared spectroscopy (VISIR), Remote Micro-Imaging (RMI) and sound recording (MIC). To guarantee the proper measurement conditions of the different techniques, a complete set of calibration targets have been included in SuperCam.

The SuperCam instrument is composed of several subsystems: The Body Unit (BU), located inside the body of Perseverance, contains the three spectrometers used for LIBS, Raman and Luminescence as well as the VIS range used for passive spectroscopy, as detailed in a previous publication [3]. The Mast Unit (MU), located on the top of the mast, above MastCamZ and Navcam cameras, includes the laser, focusing and collection optics, the microphone, the imager and the IR spectrometer as described in Ref. [4]. The third subsystem, the Calibration Target (SCCT), is located on the rover deck and contains standards for imaging and geochemical calibration, as well as spectral standards as described in a recent paper [7].

The SuperCam Calibration Target (SCCT) is made up of a collection of samples built to satisfy the calibration requirements associated with the above mentioned techniques. The different kinds of targets included to help in the calibration of spectrometers and in the chemical calibration, from which the identification of elements, mineral phases and organic compounds will be performed using the LIBS, VISIR, Raman and Luminescence spectroscopy responses, are summarized in Table 1 of [7].

Focusing on the calibration needs of these techniques, the spectral range of LIBS (245–860 nm) requires the need for the presence in the SCCT of a dedicated sample to calibrate the wavelength of the spectrometers [8]. This wavelength calibration capability for the spectrometers is provided by the titanium plate (Table 1, target 33 in Ref. [7]). Due to the detection limits of LIBS, the SCCT has several natural geologic samples (Table 1, targets 7–28 in Ref. [7]) to build in-situ calibration curves to make them adjustable to the different environmental conditions that may affect LIBS measurements. The elemental composition of such geologic samples, their spectral characterization (LIBS, Raman, VISIR and RMI) and details about their manufacturing process are given elsewhere [9].

Visible and infrared reflectance spectroscopy introduces additional calibration requirements. Indeed, to utilize the incident solar spectrum, white and dark reference targets are needed to accurately estimate the reflectance of the samples (Table 1, samples 1 and 2 in Ref. [7]).

The Raman and luminescence emissions are collected by the transmission spectrometer covering the visible range. In the case of Raman spectroscopy, changes in temperature have a slight effect on the actual wavelength of the beam emitted by the laser source. The accurate knowledge of the emitted wavelength is accomplished by the diamond target (Table 1, sample 32 in Ref. [7]) because the Raman wavenumber of diamond does not change with temperature and is accurately known. Additionally, an organic target has been included (Table 1, sample 6 in Ref. [7]) for which the Raman spectrum is accurately known. The organic target is used to test organic detection on Mars and to take periodic Raman measurements as a reference to detect any chemical change due to the environmental impact on the organic structure of the target.

The LIBS measurements allow us to identify the elements present in the samples under analysis on Mars and to check their concentrations using the chemical calibration model for each element. The complementarity between the vibrational activity selection rules of Raman and VISIR reflectance bands allows us to identify many different mineral phases including carbonates, sulfates, silicates, phosphates, oxides and hydroxides, as well as potential organics. Representative geological samples of these mineral groups, prioritizing the selection of mineral phases that are expected to be found at the Jezero landing site, have been included in the SCCT [9] for attaining the mission objectives.

To meet such calibration needs, the calibration samples must fulfill other technical requirements. Among those, the most important ones are the accurate chemical and mineralogical composition and reproducibility, as well as the homogeneity at the relevant scale for analysis. This last requirement is driven by the LIBS laser spot (≥250 μm depending on the distance to the analyzed rock or regolith in Mars) as it is the lowest in diameter of the concentric focused areas under analysis together with Raman and VISIR (diameter of LIBS < (Raman, VIS) < IR; Fig. 50 of [4]).

This paper aims to describe the work done on the selected samples included in the SCCT to guarantee the homogeneity and reproducibility of the geological targets. The starting hypothesis considers that to minimize the overall uncertainty ($\%RSD_{overall}$), which comes from the uncertainties due to the sample heterogeneity ($\%RSD_{sample}$) and the uncertainty due to the analytical response of the spectroscopic device ($\%RSD_{instrument}$), the homogeneity of the calibration targets must be as high as possible to guarantee a sample uncertainty much lower than the uncertainty due to the analytical response of the spectrometers, i.e. $\%RSD_{sample} << \%RSD_{instrument}$ [10]. In this way, the uncertainty in the concentration values assigned to the unknown samples analyzed on Mars will be only that coming from the particular working conditions of the spectrometers at the moment of performing the analyses.

$$\%RSD_{overall} = \%RSD_{sample} + \%RSD_{instrument}$$

Some of the methods proposed here allowed measurement of the uncertainty in different production batches of reference materials [11], being able to define the uncertainty within subsamples and the uncertainty between subsamples. This fact will be crucial since six subsamples of the same calibration target were manufactured for the SCCT. Other works have been inspired in a similar methodology to obtain reference materials from secondary sources [12].

2. Experimental

The description of the geological calibration samples integrated in the SuperCam Calibration Target (SCCT) has been included elsewhere [7]. Most of those samples were sintered following the procedure proposed elsewhere [13]. The targets for the calibration of minor elements were manufactured as glasses doped with known amounts of such elements, following a procedure described previously for the calibration target of the ChemCam instrument onboard the Curiosity rover [14], ending with the sintering step. The chemical compositions of the different calibration targets are described elsewhere [9].

For each target, several replicas (subsamples) were manufactured having similar compositions. All the replicas were checked for physical and chemical homogeneity. Only those replicas showing the best homogeneity were selected for their integration in the FM, FS and EQM (Flight Model, Flight Spare Model and Engineering Qualified Model) SCCT holders.

To adequately characterize the chemical elemental and mineral homogeneity, high-resolution spectroscopic techniques were selected. The elemental homogeneity was ascertained with X-ray Fluorescence imaging and micro X-ray Fluorescence spectroscopy at the scale of 100 × 100 μm. Then elemental homogeneity was tested with a LIBS setup in a Martian Chamber at a scale of 300 μm in diameter, as well as with the spare model of the ChemCam instrument at the scale of 300 μm in diameter, also in a Martian chamber. The mineral homogeneity was tested with micro-Raman confocal spectroscopy and Raman Imaging at the scale of 100 × 100 μm only for samples giving a positive Raman response because some of the samples yielded a luminescence background that inhibited the clear observation of the Raman signals.

2.1. *Micro Energy Dispersive X-ray fluorescence (μ-EDXRF) microscopy and imaging at the UPV/EHU*

Micro Energy Dispersive X-ray Fluorescence (μ-EDXRF) measurements were performed using a dual EDXRF spectrometer (M4 TORNADO, Bruker Nano GmbH, Germany) located at the University of the Basque Country (UPV/EHU). The X-ray tubes implemented in this instrument are two microfocus side window Rh tubes powered by low-power HV generators and cooled by air. One of the tubes is mounted with a 1 mm mechanical collimator. However, to verify the homogeneity of the standards included in the SCCT, the Rh- tube connected to polycapillary optics was selected, achieving lateral resolution down to 25 μm (from 17 μm at 2.3 keV to 32 μm at 18.3 keV). This tube can work between 10 and 50 kV and 100–600 μA. All the measurements were conducted at the maximum voltage and current. The detection of the fluorescence radiation was performed using an XFlash Silicon Drift Detector (SDD) with 30 mm^2 sensitive area and energy resolution of 145 eV for Mn−K$_\alpha$ line. To improve the detection of the lightest elements, primary filters between the source and the sample were not used and the measurements were acquired under vacuum. For that purpose, a MV 10 N VARIO-B diaphragm pump was used to establish a vacuum (≤20 mbar) inside the chamber of the instrument.

For the focusing of the area under study, a three-camera system was used. One camera is in the entrance of the chamber and allows overviews of the sample chamber like a fish eye. The other two cameras provide a view perpendicular to the sample surface with different magnifications. The low magnification displays an area of approx. 15 × 11 mm^2 and the high magnification 1.5× 1.1 mm^2.

Regarding the EDXRF spectra acquisition, the instrument acquires data following a single point, multi-point or auto-point strategies or programming lines or mappings of the surface under study. To verify the homogeneity through μ-EDXRF spectroscopy, single point, auto-point and mapping analyses were conducted. The energy calibration was performed before each measurement batch using the K$_\alpha$ line of Zr.

2.2. *Raman micro-spectroscopy and imaging at the UPV/EHU*

The Raman equipment used to perform the mineral homogeneity experiments at the University of the Basque Country (UPV/EHU) consists of two different setups. Single point Raman spectra were collected with a confocal micro-Raman instrument (inVia Reflex model by Renishaw, UK). This device is equipped with a continuous 532 nm excitation diode laser, as that is the excitation wavelength of the pulsed laser used in the Raman spectrometer of SuperCam, a CCD detector (Peltier cooled) and an 1800 line-pairs/mm grating. The nominal power of the laser can be modulated from 0.0001% to 100% of its maximum power in order to avoid thermal decomposition of the sample. The spectrometer is coupled to a confocal DMLM Leica microscope and different objectives of 5x, 20x and 50x were used. This microscope has a camera coupled for a perfect focusing of the laser spot on the sample. In addition, analyses were performed on a vibration-isolated table and the instrument is equipped with a class 1 enclosure to minimize spurious signals or sun light effects. The mean spectral resolution was around 1 cm^{-1} and the spectral range covers the 100-4000 cm^{-1} region. Instrument calibration was performed twice a day with a silicon slice, using its 520.5 cm^{-1} band. The software used for data collection was the Wire 4.2 (Renishaw, UK). Additionally, the laser beam was centered twice per day to ensure a proper analysis.

The Raman Imaging analysis was performed with a High Resolution Stream Line device coupled to the inVia Reflex Raman instrument. The applicability of this imaging technique for geological samples has been described elsewhere [15,16]. This setup uses a line of laser light allowing performing large Raman images in a very short time. This fast speed in acquiring the Raman images is based on the fact that as the motorized stage moves the sample beneath the microscope, the spectrum associated with a point on the sample moves across the detector. The signal on the detector is swept across the detector at the same rate, accumulating all the time, and is read out when it reaches the edge of the detector. In this way, the system allows a continuous reading by the detector as the line is rastered across the sample. Once the instrument was calibrated and centered, a Raman imaging of the whole surface of each calibration target was performed in less than 4 h by using the same continuous 532 nm laser. For the Raman image, a measurement time of 5 s and one accumulation were set up and a step between pixels of 100 μm using a 5x objective was used. All the analyses were performed at 10% of the laser power to avoid sample damage and structural or chemical changes. These integration parameters were optimized considering the signal-to-noise ratio and minimizing the exposure times required for the analysis.

2.3. *LIBS inside a Martian Chamber at the UMA LaserLab*

A Q-Switched Nd:YAG laser (Brilliant model, from Quantel) was used as the excitation source of the LIBS setup, that was used at UMA-LaserLab of the University of Malaga, to check homogeneity of the SCCT samples in Martian conditions with the same technique that will be used on Mars. The most relevant specifications of this laser system are summarized in Table S1 of the Supplementary Material. To meet the laser pulse energy level of 14 mJ deposited over the surface of the samples high-energy (300 mJ) laser pulses were attenuated using a high-energy variable attenuator (model M-935-5-OPT by Newport). In particular, for the experiments carried out, laser repetition rate was fitted to 3 Hz (more rigorously to F/07 = 2.85 Hz). At the output of the attenuator, the components of the optical assembly for guiding the outgoing laser pulses were set at an exact distance of 156 cm towards the targets deposited inside a Martian environment simulation mini chamber. Under this configuration, a circular spot size on the target of ≈300 μm in diameter was achieved, entailing therefore an irradiance of 1.8 GW cm^{-2}, on considering the laser pulse energy of 14 mJ used.

Light emitted from the emerging plasmas was collinearly collected using a confocal optical design. This geometry exploited L_1 to collect the optical emissions from the laser-produced plasmas. Once light of the plasma source passed back through the glass viewport it was collimated with L_1 towards the surface of the dichroic mirror $-M_2-$. Then the parallel light passed through the dichroic mirror and entered a plano-convex lens $-L_2-$ (25.4 mm in diameter and 75.0 mm focal length by Thorlabs). Finally, diverging plasma light was changed from a point source into a parallel beam using a collimator to form an homogeneous plasma image at the tip of the optical fiber. For optical signal examination, the collected plasma light was guided up to the entrance of a spectrograph. A *Czerny-Turner* multi-channel fiber optic spectrometer (model AvaSpec-2048-USB2-RM, 75 mm focal length, 2048 pixel CCD detectors by Avantes BV) was chosen to provide high-resolution over a broad spectral range for the emission signals. The enclosure option considered consisted of a 9-inch desktop housing for up to 4 CCD detectors (*Detector 1*, bandwidth from 237 nm to 349 nm, grating of 2400 lines/mm –blazed at 250/300 nm– deep UV-coating and 0.07 nm FWHM; *Detector 2*, bandwidth from 343 nm to 597 nm, grating of 1200 lines/mm –blazed at 500 nm– and 0.14 nm FWHM; *Detector 3*, bandwidth from 594 nm to 812 nm, grating of 1200 lines/mm –blazed at 500 nm– and 0.14 nm FWHM; Detector 4, bandwidth from 795 nm to 975 nm, grating of 1200 lines/mm –blazed at 500 nm–, 0.14 nm FWHM and OSF-550 – long-pass order sorting filter @ 550 nm). Each bench was also equipped with an entrance slit of 10 μm and a collection lens (DCL-UV/VIS) mounted directly on the detector array. This quartz lens increased the system sensitivity by a factor of 3–5, depending on the fiber diameter used. For this detection device a 600 μm optical fiber from Avantes was used. It consisted of a quadruple fiber-optic cable, 4 × 600 μm fibers, all four SMA terminated, total 2 m long, splitting in the middle from a single input fiber. The time-integrated acquisition of LIBS spectra emitted by laser-induced plasmas involved a time delay of 1.28 μs and an integration time of 1.1 ms.

Inside the chamber, the SCCT samples were accommodated on a homemade holder fit to a rotary motor that allowed refreshment of the sampling point. The electric motor was battery powered by a switched-mode multi-voltage power source (model NR-913-7580 by Noru) that supplied voltages from 3 V to 12 V. Thus, the refreshing rate of the sample was controlled with the output voltage applied allowing to perform individual laser shots on different points of the sample surface. For each SCCT samples, only one subsample not belonging to the FM, FS and EQM (Flight Model, Flight Spare Model and Engineering Qualified Model) assemblies was analyzed. For all these targets, 11 positions were interrogated (30 laser shots each) over an inner circumference of 6.0 ± 0.2 mm in diameter drawn in a clockwise direction on the whole surface of the sample.

2.4. LIBS like ChemCam under a Martian Chamber at IRAP

LIBS analyses were also conducted at IRAP (Institut de Recherche en Astrophysique et Planetologie) in Toulouse, France, using a ChemCam replica. ChemCam has used the Laser-Induced Breakdown Spectroscopy (LIBS) technique on board the MSL Curiosity rover since 2012 [5,6]. ChemCam is sensitive to all major elements (Si, Ti, Al, Fe, Mn, Mg, Ca, Na, K) and is also used to detect some minor and trace elements such as Li, Sr, Ba, Rb, Cr, F, Cl, Ni, P and Zn [17–23].

ChemCam is composed of two parts: the Mast Unit (MU) and the Body Unit (BU) which are connected by an optical fiber. The MU contains a Nd:KGW laser at 1067 nm along with a 110 mm telescope in order to focus the laser on the target and to collect the plasma light. It also contains the camera and electronics [6]. Inside the rover, the BU contains the spectrometers along with the electronics to communicate with the rover. There are three spectrometers that cover from 240 to 905 nm spectral range, with a resolution of 0.15 nm for UV (240–340 nm), 0.2 nm for violet-blue (385–465 nm) and 0.6 nm for the visible and near infrared range (470–850 nm) [5].

The ChemCam replica in Toulouse consists of a MU from the Engineering and Qualification Model (EQM) and a BU from the Engineering Model (EM). The MU is in a thermal chamber at −10 °C, where it has the best energy, around 12 mJ on the target. The BU is at ambient temperature. All the parameters are the same as for the Flight Model of ChemCam: the laser pulse duration is around 6 ns, with a 3 Hz frequency. The integration is fixed at ~3 ms. The spot size on target depends on the distance and is around 350 μm on this setup [6]. For every target, a single shot removes about a microgram of material, or about 1 μm in depth.

Targets were placed in a chamber that mimics the Martian environment: 7 mbar of a Martian atmosphere (1.6% Ar, 2.7% N_2, and 95.7% CO_2). The calibration targets on Mars are around 1.56 m from SuperCam. Therefore, the Mars chamber was placed as close as possible to the instrument, but the closest was at 1.7 m.

Four of the six replicates per target were analyzed: the FM and FS (Flight Model and Flight Spare) were not sampled in order to not damage their surface, even though the LIBS spot size is sub-millimetric. For all these targets, nine observations of 30 shots each were performed, randomly distributed.

3. Analytical procedures for assessing homogeneity

The requirement of the SuperCam instrument to guarantee reproducible measurements stated that calibration samples must be homogeneous at the 100 × 100 μm spot sizes. If samples are homogeneous at this spot size it would be homogeneous at the calibration distance in the rover, where analytical footprints will be around 300 μm in diameter for LIBS and 1150 μm in diameter for Raman. Hence, the single point EDXRF and Raman analyses were performed at these spot sizes and the corresponding percent relative standard deviation (%RSD) of the mean (EDXRF or Raman) values were used to evaluate the homogeneity for each measured subsample (the so called "within subsample homogeneity").

As several (five or six) replicas were considered for each sample of the SCCT, it was possible also to evaluate the uncertainty between samples (the so called "between subsample homogeneity") following the procedure proposed by van der Veen et al. [11].

3.1. Energy Dispersive X-ray fluorescence (EDXRF) microscopy and imaging

The first step in the EDXRF analyses was to obtain maps of elements distributed all along the surface (10 mm in diameter) of each calibration target. If an element is homogeneously distributed, its map will show a regular distribution for all the grains in the surface. However, if it is not homogeneously distributed such regular distribution will not be observed and hot spots will appear instead. As an example, Fig. 1 shows such images for the 6 major elements of the LBHVO20406 subsample where regular distributions are observed, while Fig. 2 shows those for other major and minor/trace elements where hot spots are clearly shown, suggesting a non-homogeneous distribution for such elements.

A first qualitative and visual assessment of homogeneity is derived from these EDXRF images. When in the distribution map of a specific element, the intensity of the colour used to represent the intensity of its K_α line is uniform all along the surface, the distribution of this element in the analyzed area could be considered homogeneous at the lateral resolution offered by the μ-EDXRF spectrometer. This is the case for Si and Al in Fig. 1, and also for Fe, Ca, K and Mn, in the LBHVO20406 subsample. However, when the image of an element shows randomly distributed hot spots (highly intense dots), the absence of homogeneity is considered as the main hypothesis for the distribution of that element within the whole sample, as it is observed for Cr and Cu in Fig. 2 for the

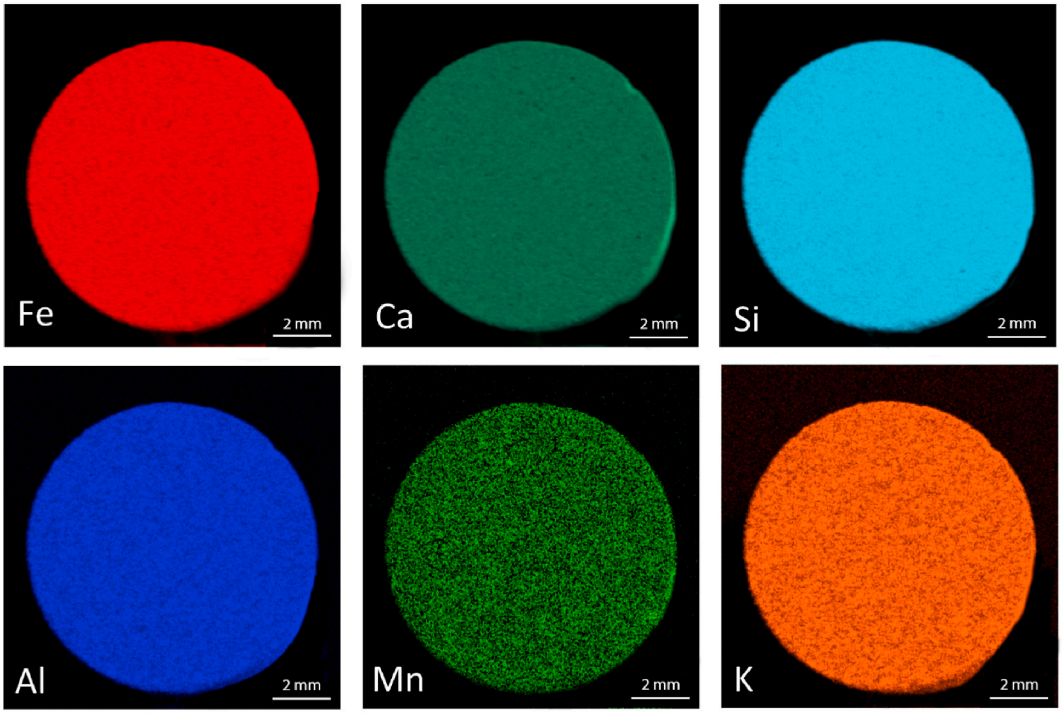

Fig. 1. EDXRF Image of the major elements in the LBHVO20406 subsample showing the homogeneously distributed elements (Fe, Ca, Si, Al, Mn and K). No significant hot spots were observed. The images show in the right-down part of the sample the EDXRF view of side due to the angle of the detector; these signals are not used to compute the average distribution of elements on the surface of the samples.

minor elements in the same subsample; this hypothesis must be further checked by quantitative measurements and %RSD evaluation.

The minor elements can show homogeneous distribution although the EDXRF signal is low. This is the case for Sr, Ti and Mg in the LBHVO20406 SCCT sample (Fig. 2). For other elements the appearance of randomly distributed hot spots can be an indication of heterogeneity (that must be confirmed after statistical calculations), as for Cr and Na. However, when the small size hot spots are alone (the applied criteria considered the distance from hotspots higher than 500 μm) and/or only in some areas of the image, the absence of homogeneity is clear for those

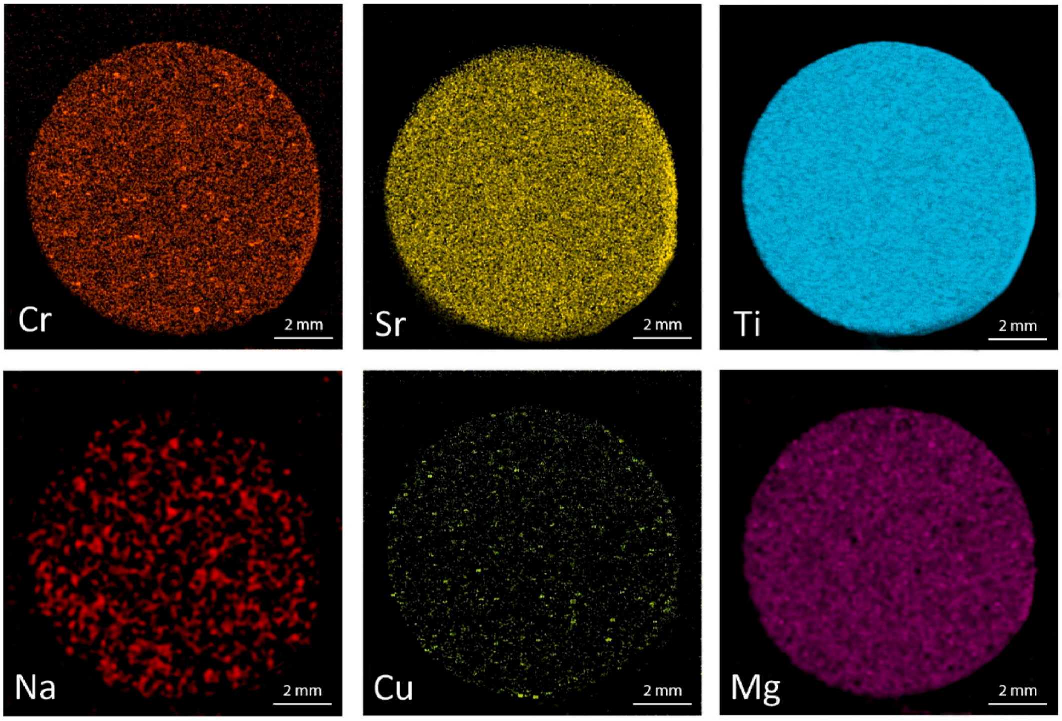

Fig. 2. EDXRF Image of the minor elements in the LBHVO20406 sample showing the homogeneously distributed elements (Sr, Ti and Mg) and those randomly distributed as hot spots (Cr and Na) or very few concentrated in parts of the surface (Cu).

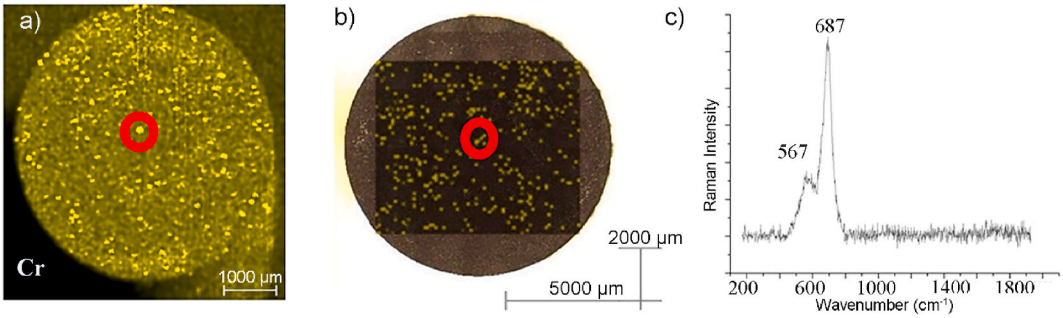

Fig. 3. The Cr hot spots detected by XRF Imaging on the TSERP0103 subsample are then checked by Raman spectroscopy (magnesium chromite in this case) and then the Raman Image is performed using its main signal at 687 cm^{-1}. Magnesium chromite is one of the minor minerals in this target.

elements, like Cu in the LBHVO20406 SCCT sample.

The elemental (EDXRF) and molecular (Raman) spectra of these hot spot were used to identify the mineral phases that generated the mentioned heterogeneity in the SCCT samples. For example, as can been seen in Fig. 3, the hotspots detected for Cr by EDXRF imaging in the TSERP0103 subsample were measured by Raman micro-spectroscopy obtaining the Raman spectrum of magnesium chromite ($MgCr_2O_4$, bands at 567 and 687 cm^{-1}). To confirm this, Raman imaging analysis can be performed searching for the main signal (in this case at 687 cm^{-1}); if the assumption is true, the mineral map showing the distribution of magnesium chromite and the Cr map must be correlated, as shown in Fig. 3.

These hypotheses about heterogeneities must be quantitatively and statistically confirmed. For that, this work uses the normalized percentage in weight (% w/w) directly offered by the software of the instrument. The obtained values cannot be considered the quantitative concentration of the elements. Rather, we prefer to use the term % Abundance for those numerical values in the sense that they represent the relative amount of the element in the whole surface of the sample. The %Abundance values are only used for the comparison among the different subsamples of the same calibration target. The sum of % Abundances is always 100% within a given uncertainty.

The EDXRF technique in the used configuration cannot detect elements such as C, O, H or N. In consequence, the %Abundance of the elements cannot be considered as a direct measure of their concentrations. Obtaining %Oxide concentration (% w/w) from %Abundance of elements requires a previous chemical calibration for the given matrix under study. As the homogeneity calculations can be done directly on the %Abundance values, it was not considered necessary to perform a calibration process to translate to %Oxide concentration values.

The estimation of the average of %Abundance was performed after optimizing the size of the spot areas, the acquisition time and the number of randomly selected spot areas to obtain reproducible values when an element is homogeneously distributed.

The minimum size of the µ-EDXRF area under analysis is 25 × 25 µm. Tests with 1 pixel (25 × 25 µm), 2 × 2 pixels (50 × 50 µm) and 4 × 4 pixels (100 × 100 µm) were performed on the surface of the SCCT targets. As the grain size of most of the targets are larger than 50 µm, the only relatively homogeneous results were those obtained from 100 × 100 µm. Afterwards, the acquisition time was optimized performing tests at 150, 125, 100, 75 and 50 s on 100 × 100 µm areas, concluding that the signal-to-noise ratio was acceptable for acquiring each point/pixel during a span of 50 s. For that condition, the variation in the Limits of Detection of each element for all the SCCT samples can be considered negligible. Finally, tests with five, ten and twenty areas of 100 × 100 µm were performed. Fig. 4 shows an example of this test with ten random areas. The optimization showed that 20 measurements are needed to guarantee a representative abundance, especially for the less abundant elements.

3.2. Raman micro-spectroscopy and imaging

Before analyzing semi-quantitatively the obtained Raman spectra, some common pre-treatment procedures were applied systematically to the whole dataset. First, a baseline correction was performed to avoid luminescence contributions; this correction was carried out automatically, after optimization tests, using a 5th order polynomial fit performed by Wire 4.2 software to accomplish a systematic procedure avoiding user errors. Then, a noise filtering was carried out by using the same Wire 4.2 software in order to reduce the level of random noise; the filtering was performed using multivariate analysis methods such as the principal component analysis (PCA). In addition, cosmic ray features were removed for the whole dataset. The removal of spikes was carried out by using a nearest neighbor procedure which consisted of

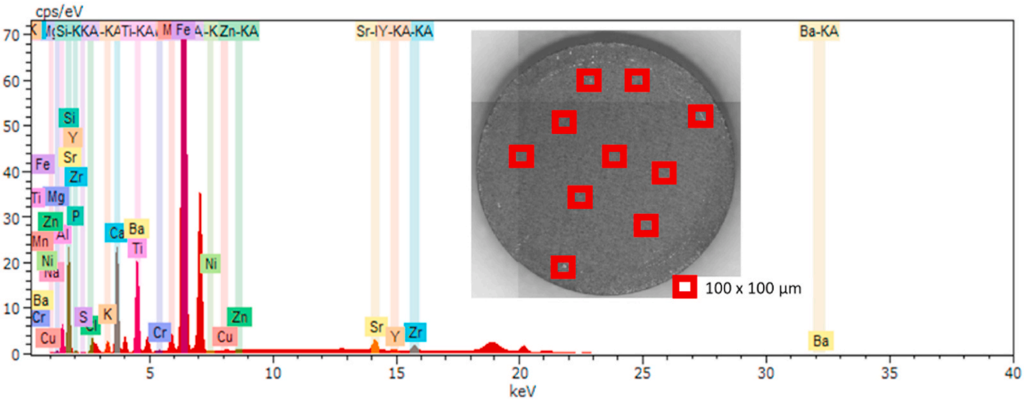

Fig. 4. The overall XRF spectrum obtained after the analyses of 10 areas of 10,000 µm^2 (100 × 100 µm) on the LJSC0104 subsample of the SCCT. The %Abundance values are obtained based on that spectrum.

determining correlation coefficients for each spectrum with all its spatial neighbors in order to select the most similar neighbor spectrum.

Once the Raman dataset was properly pre-treated, chemometric analyses were performed for the validation procedure. For this, 25 square areas of 100 × 100 μm were randomly selected from the whole surface. In each square area, a Direct Classical Least Squares (DCLS) algorithm was used for approximating the spectrum of each pixel in the map by combining different scaled copies of reference spectra of all the compounds detected in the calibration target under analysis. The scaling factor is automatically selected to fit as well as possible the spectra of the Raman map in the square area. To perform the best fit, the reference spectrum of each compound on the surface was recorded at exactly the same experimental and instrumental conditions. After that step, a quantification of the different compounds present in the sample was carried out following a Fraction Estimation procedure. Thus, a percentage of each phase present in the square area was obtained from the fit performed by DCLS.

As an example, Fig. 5 shows the case of the PMIEN0604 subsample of the enstatite calibration target. The sintering process sometimes leaves traces of the carbon used in sintering the mineral grains. This carbon is only superficial and is not present over the entire surface. In this sense, it could be considered not homogeneously distributed according to the established criteria.

Enstatite ($MgSi_2O_6$) was the main compound detected in this series with a relative abundance of around 99.7% in the total surface of the target. Microcline was detected through its main Raman bands at 236, 340, 399, 525, 683, 750, 857, 931 and 1012 cm^{-1}. Using the Raman features described by Ref. [24], we can estimate that this calibration target is composed of 87% pure enstatite ($MgSi_2O_6$) and 13% ferrosilite ($Fe_2Si_2O_6$). The specific characterization of the target compounds, provided by the Raman peaks, are of great help interpreting minerals composed of mixtures of two end-members.

Raman imaging, apart from the semi-quantitative data, also helped in the understanding of the molecular spatial distribution in the calibration targets. In Fig. 5 as well, it can be seen how the En87 Fs13 is homogeneously distributed over the entire surface of the sample.

Something similar happened in the series PMIFA030x, where olivine ((Mg,Fe)2SiO4) was detected as the main compound (Fig. 6). Olivine was identified using its main Raman bands at ≈820 and ≈ 850 cm^{-1}. By using these Raman bands, the actual composition of the olivine present in the entire calibration target could be calculated. For this calculation, a methodology developed by the IBeA research group of the University of the Basque Country was employed [25,26]. By this means, forsterite (Mg2SiO4) – fayalite (Fe2SiO4) ratios, varying from $Fo_{58\text{-}72}$ and $Fa_{42\text{-}28}$, were detected in the different replicas of the same series.

The replicas appear to be molecularly homogeneous for olivine in most of the samples (1, 2, 3 and 4) showing a relative presence of around 95%. However, small particles of pyroxene were also detected (always with a relative abundance lower than 5%). The distribution of these particles was heterogeneous, without affecting the homogeneous

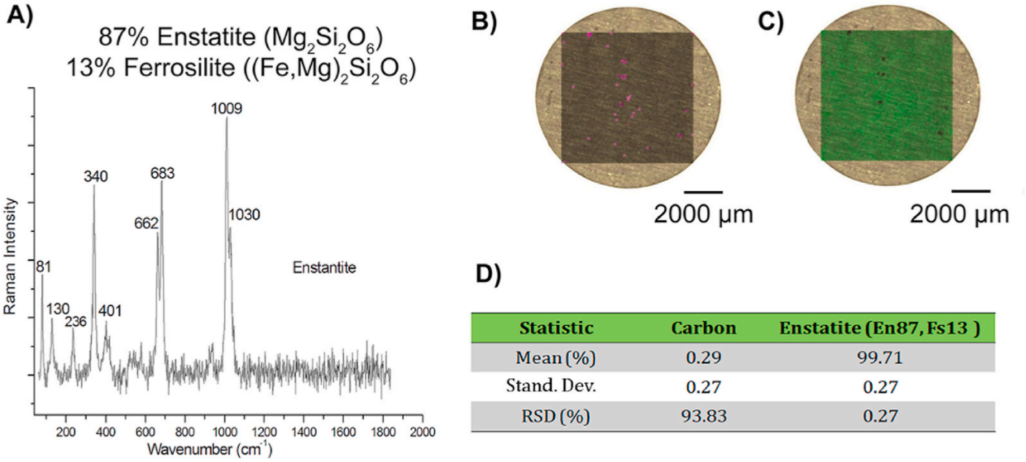

Statistic	Carbon	Enstatite (En87, Fs13)
Mean (%)	0.29	99.71
Stand. Dev.	0.27	0.27
RSD (%)	93.83	0.27

Fig. 5. Raman spectrum of the PMIEN0604 subsample (enstatite) and quantitative abundance by Raman Imaging analysis.

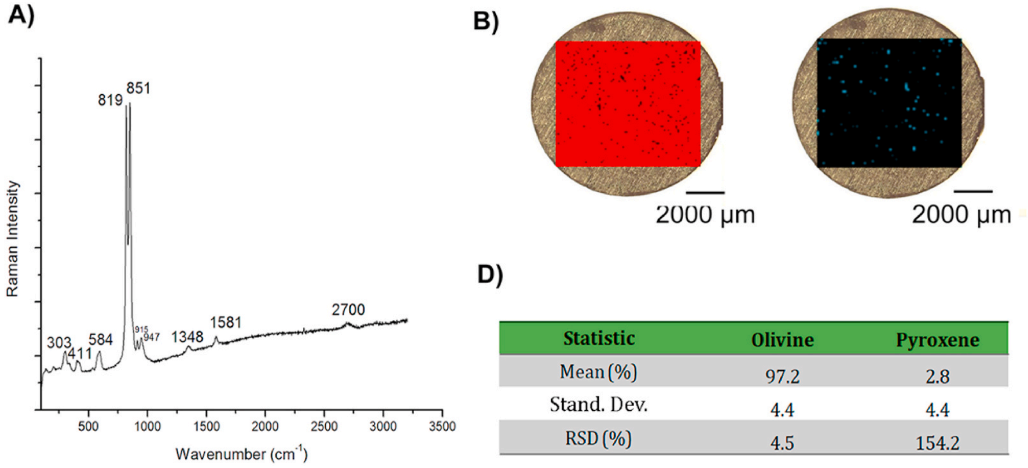

Statistic	Olivine	Pyroxene
Mean (%)	97.2	2.8
Stand. Dev.	4.4	4.4
RSD (%)	4.5	154.2

Fig. 6. Raman spectrum of a pure grain of olivine (traces of carbon are also present), without any signals of pyroxene. Raman images of olivine and pyroxene together with their mineral distributions for the whole surface of the PMIFA0301 subsample of the SCCT.

distribution of olivine (Fig. 6), except for subsamples 5 and 6, where olivine also appeared to be molecularly heterogeneous (RSD%>15%).

The above description shows good calibration targets for just one compound. Some other calibration targets were found to be homogeneous for more than one mineral phase. This is the case of LCMB000x series that will be described in the next section.

3.3. Quality procedures on EDXRF and Raman data

EDXRF %Abundance data obtained in twenty random 100 × 100 μm areas in each subsample were used to calculate the average of %Abundance, its standard deviation and the %RSD values for each element per subsample. The average and standard deviation of the results corresponding to all replicas, along with the individual averages and relative standard deviations (%RSD) are shown in Table 1.

The %RSD values provide information about the variability of the average concentrations found in the replicas of each of the SCCT targets. Low %RSD values would mean similar abundances for all the analyzed replicas. However, these results can provide more useful information. On the one hand, variability of the results of the analyzed elements of interest in each of the replicas can give a way of selecting the best replica regarding the dispersion. This can be carried out calculating the Root Mean of Squares (RMS) of the %RSDs of those elements in each replica. The lowest RMS value would mean the lowest overall dispersion of the results considering the elements of interest in each of the replicas. On the other hand, calculating the RMS of the %RSDs of each of the elements analyzed in all the replicas provides information regarding the average dispersion of the results of each element in all the replicas as shown at the bottom of Table 1. This is useful as a worst-case scenario that can be expected with the variability of each element in each of the samples at the sample size used in the measurements.

The averages for each five replicas of the LANKE010x SCCT target are plotted as an example, together with their standard deviations as uncertainty bars, in Fig. 7, where the X-axis corresponds to each five replicas of the LANKE010x series. This is another way of checking quantitatively the homogeneity of the different elements. As seen, not all the standard deviation values are statistically comparable. The LANKE0102 replica (position 2 in Fig. 7) presents the highest error for the major elements and also the mean value of %Abundance does not match with the mean values of the other four replica. Thus, the

Table 1

Mean %Abundance of 20 points, standard deviation and RSD values for each element in the five ankerite replica (uncertainty within sample). The Root Mean Square of the %RSD values is given as the uncertainty between subsamples. The values highlighted in bold correspond to homogeneously distributed elements in the LANKE01 target. LANKE0101 is the target in the SCCT currently on Mars.

	%Abundances	**Mg**	**Al**	**Si**	**S**	**K**	**Ca**	**Mn**	**Fe**	**Cu**	**Zn**	**Sr**
LANKE0101	**Mean**	16.1	0.13	11.0	0.0216	0.135	52.1	0.969	19.0	0.0064	0.0313	0.0348
	Dev	1.1	0.13	4.1	0.0068	0.084	2.1	0.059	1.3	0.0026	0.0062	0.0021
	%RSD	6.8	103	37	32	62	4.0	6.9	7.0	49	19	6.0
LANKE0102	**Mean**	15.0	0.074	16	0.024	0.106	50.2	0.911	17.1	0.0052	0.0243	0.0319
	Dev	3.0	0.059	10	0.01	0.05	6.1	0.093	1.7	0.0025	0.0026	0.0026
	%RSD	17	79	64	41	47	12	9.8	10	49	11	8.2
LANKE0103	**Mean**	15.7	0.087	13	0.0169	0.121	51.2	0.948	18.3	0.0072	0.0269	0.0346
	Dev	1.5	0.045	5	0.0085	0.051	2.4	0.042	0.84	0.0014	0.002	0.0014
	%RSD	9.7	51	34	50	43	4.6	4.4	4.6	20	7.3	4.0
LANKE0104	**Mean**	16.2	0.069	11.1	0.042	0.121	52.9	0.944	18.3	0.0059	0.0281	0.033
	Dev	1.3	0.039	4.4	0.024	0.026	2.5	0.054	1.3	0.0023	0.0027	0.0024
	%RSD	7.8	56	39	57	22	4.6	5.8	6.9	39	9.6	7.2
LANKE0105	**Mean**	16.0	0.098	12.9	0.033	0.102	51.4	0.954	18.6	0.0068	0.0292	0.0329
	Dev	1.9	0.093	6.4	0.016	0.036	3.3	0.066	1.2	0.0025	0.0034	0.0021
	%RSD	12	95	49	47	36	6.4	6.9	6.6	36	12	6.3
	Averaged Values	**Mg**	**Al**	**Si**	**S**	**K**	**Ca**	**Mn**	**Fe**	**Cu**	**Zn**	**Sr**
	Mean	15.8	0.092	12.8	0.0275	0.117	51.5	0.945	18.24	0.00630	0.0280	0.03344
	Dev	0.75	0.038	2.4	0.0070	0.022	1.6	0.019	0.45	0.00049	0.0017	0.00045
	%RSD	4.8%	42%	19%	26%	19%	3.1%	2.0%	2.4%	7.8%	5.9%	1.4%
RMS of the %RSD values		**10.8**	67.5	45.1	50.3	33.7	**6.44**	**6.53**	**6.99**	36.9	**9.74**	**6.61**

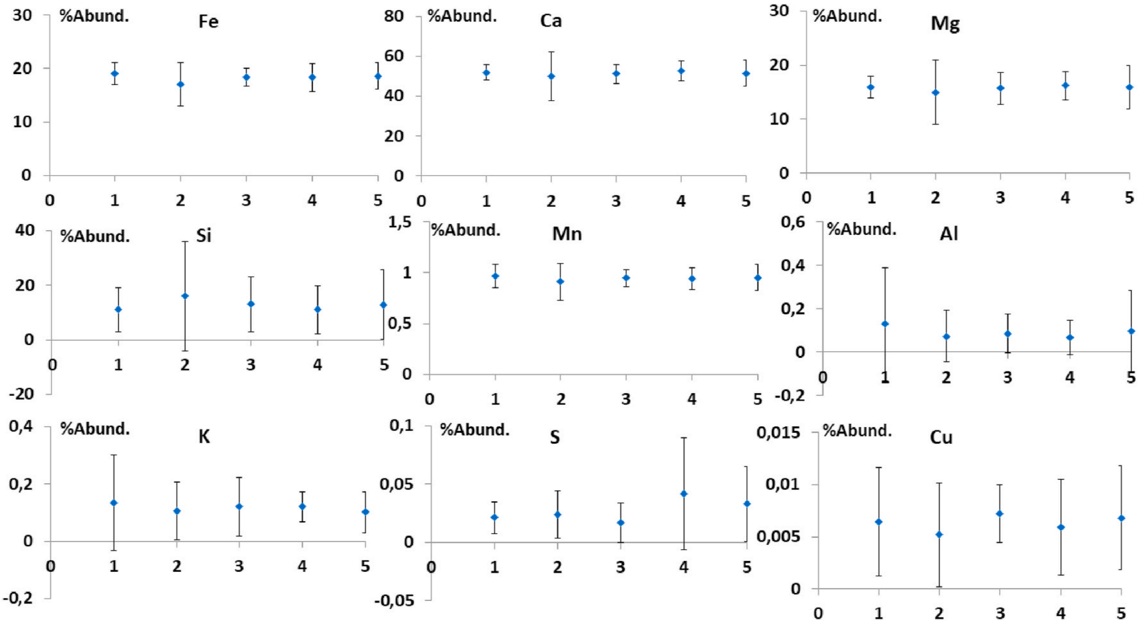

Fig. 7. %Abundance values, with their uncertainties as error bars, for each element in the five subsamples of ankerite obtained by EDXRF. Point 1 belongs to the sample included in the SCCT Flight Model currently on Mars.

LANKE0102 replica can be considered out of the statistical distribution of the other four replicas and should be discarded for its inclusion in any of the SCCT models. For this target, the LANKE0101 replica was selected to be included in the Flight Model (FM) assembly.

The Raman data were handled in a similar way to assess which mineral phase is homogeneously distributed in the SCCT samples. Using the percentages obtained by the Direct Classical Least Squares algorithm implemented in the software of the Stream Line coupled to the InVia Reflex Raman spectrometer, on each of the 25 square areas imaged by Raman spectroscopy for each calibration target, the mean and the standard deviation were also calculated, and then the %RSD values.

The calibration target was accepted as homogeneous, concerning the mineralogy, if the %RSD for each detected mineral phase from the 25 measurements was below 15%, as is shown in Fig. 8 for the chert (LCBM0005) SCCT target. In this case, both hematite and quartz are homogeneously distributed across the surface of the target.

3.4. Quality procedures on LIBS data

Two LIBS setups were used, one at the University of Malaga and the second one at IRAP. As the measured samples were different, the methods to estimate uncertainties were also different.

At the University of Malaga, the LIBS measurements were performed only in one subsample of each SCCT target. Radially distributed 11 measurements, with 30 laser shots each, were obtained on the whole surface of the subsamples. To obtain the intensity of the LIBS response, one line (LIBS band) was selected for each major element. With the 11 intensity values, the mean, its standard deviation and its %RSD were computed. These %RSD values were taken as the uncertainty for the LIBS measurements performed in the described setup at the University of Malaga.

For the LIBS-ChemCam at IRAP, data acquisition and processing were performed in a similar way to the EDXRF measurements described

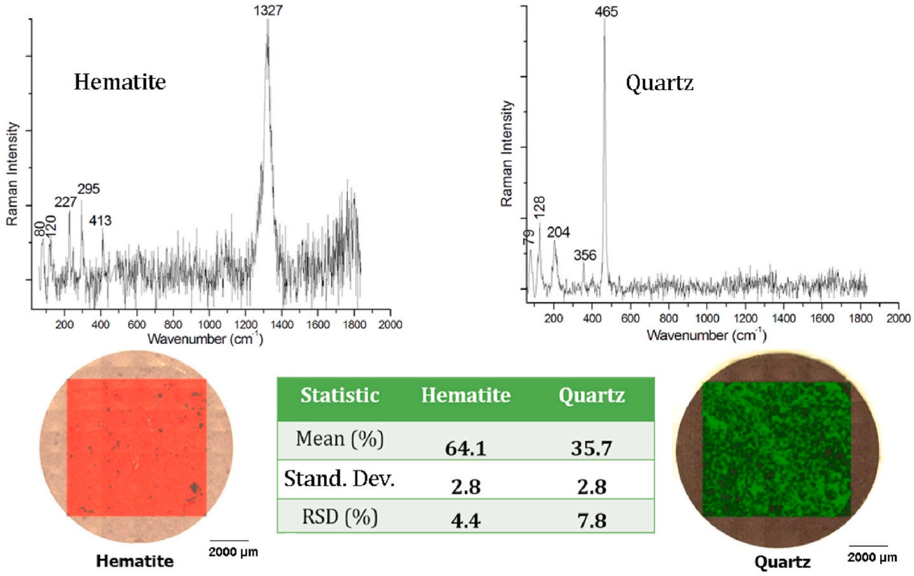

Statistic	Hematite	Quartz
Mean (%)	64.1	35.7
Stand. Dev.	2.8	2.8
RSD (%)	4.4	7.8

Fig. 8. Homogeneous distribution of hematite and quartz minerals in the chert (LCMB0005) SCCT sample, obtained by Raman image.

Table 2
Uncertainty values (RMS of the %RSD values) of the homogeneously distributed major elements for each SCCT sample obtained from EDXRF measurements. (nhd) non-homogeneously distributed. (–) below the detection limit.

RMS of the %RSD values	Na	K	Mg	Ca	Si	Al	Fe	Mn	Ti	S
TSRICH040x	nhd	12	nhd	nhd	nhd	nhd	nhd	nhd	nhd	9.0
LCMB000x	–	–	–	nhd	3.2	nhd	nhd	nhd	–	nhd
LCA53010x	–	–	15	0.8	nhd	nhd	nhd	nhd	–	nhd
PMIFS050x	–	nhd	4.7	15	2.6	15	1.0	1.6	nhd	–
TAPAG020x	–	–	–	7.4	–	–	–	–	–	–
PMIOR050x	4.9	0.9	–	–	0.2	0.3	nhd	nhd	nhd	–
PMIDN030x	–	nhd	3.6	1.4	0.6	12	2.0	2.7	7.8	–
PMIFA030x	–	–	2.1	nhd	2.2	nhd	1.8	2.7	nhd	nhd
PMIAN010x	1.4	4.4	–	1.1	0.5	0.6	1.9	7.4	nhd	–
PMIEN060x		nhd	0.9	10.6	0.6	nhd	2.0	10	nhd	–
TSERP010x	–	–	1.6	–	3.0		14.1	9.8	nhd	–
LBHVO2040x	nhd	11	14	4.1	1.2	5.5	5.3	4.7	10	nhd
LJSC1030x	nhd	nhd	nhd	9.7	3.2	6.6	5.7	11	4.8	nhd
LANKE010x	–	nhd	11	6.4	nhd	nhd	7.0	6.5		nhd
LSIDE010x	–	–	10.0	10.6	8.6	nhd	4.0	15		15
LJMN1010x	nhd	12	nhd	8.8	15	15	11	7.6	8.8	nhd
NTE01030x	–	4.0	2.4	1.5	2.0	1.4	4.4	6.8	2.7	–
NTE02010x	–	2.4	1.3	0.7	0.6	0.6	1.2	0.8	1.5	nhd
NTE03010x	9.3	4.3	2.1	0.6	0.7	1.3	0.9	9.6	1.1	nhd
NTE04010x	9.9	3.9	1.6	0.8	0.8	0.6	1.7	1.0	2.6	nhd
NTE05030x	–	5.0	2.7	2.3	1.7	1.1	7.2	2.7	2.7	nhd
SHERGO0x	–	7.8	4.0	1.2	1.9	2.4	1.9	–	nhd	12

above. Four subsamples were measured for each SCCT target. At each subsample, 9 randomly distributed points were investigated (30 laser shots each) to obtain the LIBS peak intensities using one or two signals for each major elements. From the 9 intensities obtained for each selected LIBS signals, the mean, standard deviation and %RSD values were obtained, giving the uncertainty within subsample. The procedure was repeated for the four subsamples, obtaining a set of four values that represent the dispersion between subsamples. The Root Mean Square (RMS) was then computed from the four %RSD values for each of the major elements analyzed in all the replicas. This RMS of the %RSD was considered the overall uncertainty for each SCCT target, as it provides information regarding the average dispersion of the results of each element in all the replicas.

4. Results

4.1. Elemental homogeneity through Energy Dispersive X-ray fluorescence (EDXRF) microscopy and imaging

The procedures explained above to obtain the EDXRF %Abundance results and their respective “homogeneity within subsamples” values and “homogeneity between subsamples” were applied to the five/six subsamples for all the calibration targets. The overall uncertainty was calculated from the Root Mean Square (RMS) of the %RSD between samples. Table 2 summarizes the obtained overall uncertainty (as %RSD) values with the EDXRF technique for the major elements of the 22 natural geologic samples contained in the SCCT.

These major elements were also measured by LIBS. Thus, the final suggested values for the uncertainties of the major elements are not the same as the ones collected here in Table 2, from the EDXRF tests. The final suggested values for the uncertainties will be obtained from the measured %RSD of the EDXRF and LIBS data. However, the minor elements were only measured by EDXRF and their homogeneities were evaluated following the same procedure as for the major ones.

The finally uncertainties (%RSD) suggested values for major and minor elements, due to the homogeneity of the raw materials, are summarized in Tables 6 and 7 of the Discussion section for the 22 natural geologic samples contained in the SCCT.

The homogeneity EDXRF analysis revealed that SCCT samples, intended for calibrating some given elements, fulfill the requirements (for example, TSRICH040x was intended for S and K and both elements are homogeneously distributed). In addition, as natural rocks have been used to prepare the powders for the sintering process, some other minor elements present in those geologic materials fulfilled also the homogeneity requirements. This is the case of LCA53010x (calcite, it was intended only for Ca) series, which showed adequate homogeneity not only for Ca but also for Mg and Sr.

The NTE series of glassy samples doped with minor elements requires especial attention. Due to the manufacturing process of these samples, not only the minor elements (Ni, Cu, Zn and Sr) but also some major elements (K, Mg, Ca, Si, Al, Fe, Mn and Ti) showed homogeneous distribution. In NTE03010x and NTE04010x series, Na and Ba showed a homogeneous distribution at the scale of 100 μm in diameter, being out of homogeneity at this scale in the NTE01030x, NTE02010x and NTE05030x series, with %RSD≈20%.

4.2. Elemental homogeneity with LIBS measurements for major elements

LIBS tests were performed for some of the subsamples with the aim to validate the EDXRF homogeneity results for major elements. In these tests, not all the minor elements were checked but all the majors were confirmed.

Table 3 summarizes the %RSD values for the intensity of the LIBS signals obtained with the setup at the University of Malaga. As can be seen, the major elements showing homogeneity with this LIBS setup are the same elements confirmed previously by EDXRF measurements. From the 147 analyzed elements (7 elements/sample on 21 samples, because the Shergottite sample was left out), these LIBS measurements detected 13 additional cases showing homogeneity that were not shown as homogeneous by EDXRF. Seven of the 13 were Na, observed in seven samples. It is known that Na is a light element not easily measured by EDXRF, and that the EDXRF results are not very reproducible if the concentration is not ≥10 times the detection limit. Conversely, 10 major elements at low concentration levels, considered homogeneously

Table 3
LIBS (UMA setup) study of the %RSD uncertainty values from the 11 measurements for the homogeneously distributed major elements in each SCCT sample. (nhd) non-homogeneously distributed. (–) below the detection limit.

Samples	RSD (%)						
	Si I@288 nm	Al I@394 nm	Mg III@518 nm	Fe I@404 nm	Ca I@422 nm	Na I@589 nm	K I@766 nm
TSRICH0402	nhd	nhd	nhd	nhd	nhd	ngd	15
LCMB0001	4	–	–	14	14	–	–
LCA530101	–	–	–	–	4	12	–
PMIFS0504	4	–	5	6	5	–	–
TAPAG0204	–	–	–	–	7	–	–
PMIOR0504	2	6	–	–	–	6	8
PMIDN0303	9	10	9	–	9	8	–
PMIFA0301	6	–	3	6	7	–	–
PMIAN0104	2	3	nhd	–	2	5	18
PMIEN0603	3	–	4	9	10	–	7
TSERP0103	9	nhd	5	nhd	nhd	nhd	5
LBHVO20401	4	6	9	6	6	5	13
LJSC10301	7	6	–	7	6	3	7
LANKE04	–	–	3	5	5	12	–
LSIDE04	6	–	8	8	8	–	–
LJMN10101	6	10	9	10	11	12	15
NTE010304	Nhd	8	8	nhd	10	9	–
NTE020101	5	6	6	10	8	7	–
NTE030101	7	5	4	10	6	6	–
NTE040101	4	6	5	6	4	3	–
NTE050304	7	9	9	nhd	10	8	nhd

distributed by XRF analysis, were not detected by this LIBS setup.

In the 21 samples analyzed, there were 72 cases of homogeneous distributions reported by both techniques, although the spot size of the EDXRF is much smaller than the spot size of the LIBS measurements. This agreement validates the usefulness of the EDXRF results for guaranteeing the LIBS calibrations on the SCCT samples.

Table 4 summarizes the %RSD values for the intensity of the LIBS signals obtained with the (ChemCam) setup (IRAP). As seen, the major elements showing homogeneity with this LIBS setup are the same elements confirmed previously by EDXRF measurements. From the 168 analyzed cases (8 elements/sample on 21 samples, as Shergottite was not checked), these LIBS measurements detected 20 new cases showing homogeneity that were not reported as homogeneous by EDXRF, although 6 of the 20 were Na in six samples, all coincident with the LIBS results presented in Table 4. Conversely, 6 major elements at low concentration levels, homogeneously distributed by EDXRF analysis, were not detected by this LIBS setup. On the whole, there were 88 cases of homogeneous distributions reported by both XRF and the ChemCam LIBS setup for the 21 samples considered, although the size of the spots were different.

4.3. Mineralogic homogeneity through Raman imaging

The mineral homogeneity results are based on observations of 9 targets showing adequate Raman responses from the 22 SCCT samples. These observations were made on just one of the replica sets of targets. The statistics are based on the standard deviations calculated from areas covered for each mineral in the different 100 × 100 μm squares on each sample. The Raman results showed that not only major but also minor compounds could be detected by Raman spectroscopy on those 9 targets.

Table 4
LIBS like ChemCam (IRAP) study of 21 of the 22 SCCT samples. The uncertainty values are given as RMS of the %RSD values for the homogeneously distributed elements of each SCCT sample using two different LIBS lines for most of the elements. (nhd) non-homogeneously distributed. (–) below the detection limit.

Samples	RMS of the %RSD values											
	Si I @288 nm	Si II @634 nm	Ti II @335 nm	Al I @394 nm	Mg I @285 nm	Mg II @448 nm	Fe l @404 nm	Fe II @260 nm	Ca II @397 nm	Ca I @422 nm	Na I @589 nm	Na818 @818 nm	K I @766 nm
TSRICH040x	7.2	nhd	8.0	8.4	6.2	nhd	9.0	6.1	8.6	3.5	14	–	8.2
LCMB000x	8.2	5.9	–	13	–	–	7.1	4.5	–	–	–	–	–
LCA53010x	7.7	–	–	–	3.7	–	–	–	2.9	1.7	nhd	–	–
PMIFS050x	2.7	2.6	–	–	3.9	2.9	2.6	1.9	3.2	2.8	–	–	6.2
TAPAG020x	–		–	–	–	–	–	–	–	–	–	–	–
PMIOR050x	4.8	2.3	–	11.8	–	–	–	–	–	–	3.0	6.1	2.7
PMIDN030x	3.3	2.6	–	11.6	4.2	2.8	5.4	2.9	1.5	2.0	3.7	–	13.8
PMIFA030x	5.2	3.3	–	–	6.8	4.3	3.8	2.5	11	8.6	–	–	–
PMIAN010x	5.6	2.0	–	1.3	–	–	–	–	1.3	1.7	2.9	3.5	2.7
PMIEN060x	4.9	2.4	–	5.9	4.8	3.7	2.9	2.9	7.0	5.4	–	–	–
TSERP010x	6.5	4.9	–	–	9.1	5.2	nhd	nhd	–	–	–	–	–
LBHVO2040x	4.1	3.3	4.7	2.2	6.2	6.9	4.7	2.8	1.9	2.8	4.1	6.2	5.7
LJSC1030x	4.4	3.1	4.8	3.6	8.6	nhd	5.6	3.3	3.6	2.7	3.8	7.2	6.6
LANKE010x	–	–	–	–	4.5	5.1	4.3	3.1	1.7	1.3	–	–	9.9
LSIDE010x	–	4.3	–	–	–	–	1.6	1.8	2.0	1.7	–	–	–
LJMN1010x	Nhd	6.3	8.6	3.2	4.2	6.9	5.3	4.7	2.4	3.0	6.8	9.0	3.4
NTE01030x	7.7	4.1	5.3	2.2	5.7	5.8	11	4.9	2.1	2.4	3.4	4.7	6.1
NTE02010x	3.4	2.5	9.0	1.5	6.3	3.9	2.7	3.0	1.6	1.8	2.9	4.9	3.3
NTE03010x	2.1	3.4	4.0	1.3	4.6	2.7	1.4	2.6	1.2	1.4	3.8	6.5	3.1
NTE04010x	2.1	2.4	6.7	1.6	5.0	3.0	2.4	3.2	1.7	1.2	2.6	5.9	2.5
NTE05030x	9.0	4.5	6.2	2.1	6.8	6.0	nhd	6.7	1.9	2.7	3.4	6.6	4.5

Table 5
Homogeneous distribution of minerals (by Raman) in the replicas of the SCCT targets. Only the Calibration Targets showing Raman response are included. (√) indicates homogeneous distribution. (–) indicates absence of homogeneity at the scale of SuperCam-Raman. Replica with (X) were not manufactured or approved to be tested.

Name/Replica	01	02	03	04	05	06	07	08
TSRICH040x	✓	✓	-	✓	-	✓	(X)	(X)
LCMB000x	✓	✓	✓	✓	✓	✓	(X)	(X)
LCA53010x	✓	✓	✓	✓	✓	✓	(X)	(X)
TAPAG020x	✓	✓	✓	✓	✓	✓	(X)	(X)
PMIOR050	(X)	(X)	✓	-	-	✓	✓	✓
PMIDN030x	(X)	✓	-	(X)	✓	✓	-	-
PMIFA030x	(X)	✓	✓	-	✓	✓	-	(X)
PMIAN010x	(X)	(X)	-	✓	✓	✓	-	✓
PMIEN060x	(X)	✓	✓	✓	-	✓	-	(X)

The results among all the calibration targets, showing a positive Raman response demonstrated that the level of homogeneity differed depending on the nature of the calibration targets, some of them being perfectly homogeneous for one or two mineral phases, and others less. Table 5 shows the subsamples confirming mineral homogeneity from the 9 SCCT samples with a positive Raman response. As can be seen each sample has six replica that were tested, although not all of those 6 replica shown a homogeneous mineral distribution on the whole surface of the target.

5. Discussion

The SCCT is a complex calibration assembly on board Perseverance Rover, in line with the ambitious, complex and versatile instrument that is SuperCam. The calibration of an instrument so complicated is a challenge in itself, and the design of a system that can also survive the journey and operation on Mars constitutes a greater challenge. This challenge was faced with an international effort that brought together researchers from different disciplines, covering problems from the space engineering to analytical chemistry. The resulting hardware provides a basic reference for every measurement, and this required the development and careful analysis of 22 different mineral samples for LIBS calibration, a diamond sample for Raman checking, 5 reflectance standards, an organic sample, a sample from Mars and imaging calibration targets. These 22 samples fulfill the requirements stated by the mission in terms of composition and concentration [7,9] but also they must fulfill two specific requirements: “All LIBS targets shall be assayed for major, minor, and trace elements at uncertainties typical of XRF (where applicable) or of typical laboratory measurements » and “All LIBS targets shall be characterized for heterogeneity”.

This work was developed to defined the best conditions for the fulfillment of the above mentioned requirements. The heterogeneity of the 22 mineral samples was tested, concluding that for LIBS measurements the major elements listed in Table 6 have a homogeneous distribution all along the surface of the calibration targets. The suggested %RSD values reflect the level of homogeneity of each element and calibration target at the spot size of the SuperCam-LIBS instrument and were obtained as a compromise (propagation of weighted uncertainties collected in Tables 2–4) from all the EDXRF and LIBS measurements performed in this work. For the minor elements, Table 7 summarizes the suggested %RSD, that coincide with the values calculated from the EDXRF tests as minor elements were not tested by the LIBS setups. The %

Table 7
Calculated uncertainties, as %RSD error values, of the homogeneously distributed minor elements for each SCCT samples at the LIBS spot size of the SuperCam instrument. The mark (–) means below the detection limit.

%RSD	P	Ni	Cu	Zn	Cr	Sr	Ba	Cl
TSRICH040x	–	–	–	–	–	–	–	–
LCMB000x	–	–	–	–	–	–	–	–
LCA53010x	–	–	–	–	–	7.6	–	–
PMIFS050x	–	–	–	–	–	–	–	–
TAPAG020x	9.3	–	–	–	–	–	–	3.6
PMIOR050x	–	–	–	–	–	–	–	–
PMIDN030x	–	–	–	–	–	6.9	–	–
PMIFA030x	–	7.7	–	14	–	–	–	–
PMIAN010x	–	–	–		–	3.2	–	–
PMIEN060x	–	–	–	–	–	–	–	–
TSERP010x	–	–	14	–	–	–	–	–
LBHVO2040x	–	15	14	13	14	4.0	–	–
LJSC1030x	12	–	–	7.7	–	6.6	11	–
LANKE010x	–	–	–	9.7	–	6.6	–	–
LSIDE010x	–	–	–	–	9.8	8.1	–	–
LJMN1010x	–	11	10	11	–	9.4	–	–
NTE01030x	–	4.7	3.6	1.8	6.9	7.8	12	–
NTE02010x	–	2.2	6.9	2.1	8.1	1.2	13	–
NTE03010x	–	2.0	3.1	2.2	12	2.4	5.7	–
NTE04010x	–	1.6	5.7	2.0	11	1.5	5.0	–
NTE05030x	–	4.7	7.7	2.7	15	2.9	11	–
SHERGO0x	–	3.2	–	–	–	–	–	–

Table 6
Calculated uncertainties, as %RSD error values, of the homogeneously distributed major elements for each SCCT samples, at the LIBS spot size of the SuperCam instrument. The mark (–) means below the detection limit. The mark * means homogeneously distributed minerals by Raman.

%RSD	Na	K	Mg	Ca	Si	Al	Fe	Mn	Ti	S
***TSRICH040x**	–	13	6.2	3.5	7.2	8.4	9.0	–	8.0	9.0
***LCMB000x**	–	–	–	–	8.2	13	10	–	–	–
***LCA53010x**	14	–	15	1.8	7.7	–	–	–	–	–
PMIFS050x	–	6.2	4.4	3.9	2.6	–	3.0	1.6	–	–
***TAPAG020x**	–	–	–	7.4	–	–	–	–	–	–
***PMIOR050x**	5.9	3.9	–	–	2.2	6.3	–	–	–	–
***PMIDN030x**	4.8	14	3.6	1.4	1.6	12	3.2	2.7	7.8	–
***PMIFA030x**	–	–	4.1	6.3	4.2	–	1.8	2.7	–	–
***PMIAN010x**	3.2	3.6	–	1.4	2.5	2.6	3.6	7.4	–	–
***PMIEN060x**	–	–	3.4	8.2	2.8	5.9	3.0	10	–	–
TSERP010x	–	–	3.9	–	5.2	–	15	9.8	–	–
LBHVO2040x	5.1	9.7	7.4	3.7	3.2	4.6	5.3	4.7	7.3	–
LJSC1030x	4.7	6.8	–	4.1	4.4	5.4	5.4	11	4.8	–
LANKE010x	–	9.9	5.9	2.7	–	–	4.8	6.5	–	–
LSIDE010x	–	–	9.0	3.9	5.2	–	2.5	15		15
LJMN1010x	9.3	7.7	6.7	5.0	6.3	6.6	6.7	7.6	8.8	–
NTE01030x	5.7	5.0	5.5	2.0	4.4	1.8	6.8	6.8	4.0	–
NTE02010x	4.9	2.9	4.6	1.4	2.9	2.4	2.3	0.8	5.2	–
NTE03010x	5.4	3.7	3.4	1.1	2.1	2.5	1.6	9.6	2.6	–
NTE04010x	3.8	3.2	3.6	1.2	2.3	1.1	2.4	1.0	4.6	–
NTE05030x	6.0	4.8	6.1	2.3	5.6	1.6	7.2	2.7	4.4	–
SHERGO0x	–	7.8	4.0	1.2	1.9	2.4	1.9	–	–	12

Table 8
Homogeneous distribution of minerals in the SCCT samples of the FM model and the best Raman signals for calibration purposes.

Sample	Mineral phase	Main Wavenumbers
TSRICH04	K-Sulphate	984 cm^{-1}
LCMB000	Chert	465 and 1327 cm^{-1}
LCA53010	Calcite	1085 cm^{-1}
TAPAG020	Apatite	960 cm^{-1}
PMIOR050	Orthoclase	513 cm^{-1}
PMIDN030	Clinopyroxene	666 and 1012 cm^{-1}
PMIFA050	Fayalite	doublet 820 + 851 cm^{-1}
PMIAN010	Andesine	465 and 511 cm^{-1}
PMIEN060	Enstatite	340 cm^{-1}

RSD values in Tables 6 and 7 are a measure of the homogeneity of the SCCT samples, at the spot size of the LIBS measurements at 1.56 m, the distance of the SuperCam Mast Unit to the calibration target in the Perseverance rover. Supplementary Table S2 summarizes the elemental composition of the SCCT samples, with their relative standard deviations, obtained by two quantitative techniques, Laser Ablation Inductively Coupled Mass Spectrometry (LA-ICPS) and Electron Probe Micro Analysis (EPMA) [9].

The uncertainty values due to the heterogeneity of the raw materials used to prepare the SCCT samples, collected in Tables 6 and 7 apply for all the replica included in the Flight Model (FM), Flight Spare Model (FS) and Engineering Qualified Model (EQM), which are described in Table S3 of the Supplementary Material.

Samples with the * mark are those that also show a mineral homogeneity distribution as shown in Table 5. In these nine targets valuable Raman signals were obtained that could be eventually used to validate the calibrations on Mars. These peaks (Raman wavenumbers) are given in Table 8. The most adequate samples with a positive Raman response are all located in rows 2 and 3 of the SCCT holder, simplifying the opportunities to take Raman spectra of these targets on Mars.

For these nine targets, combined LIBS and Raman calibrations can be done. Cross-calibration among the different SuperCam techniques will be interesting as it has never done before with these techniques on a planetary mission. This can be done by SuperCam with the high quality calibration targets included as one of the three important subsystems of the instrument.

6. Conclusions

The SCCT is a complex calibration assembly on board Perseverance Rover, containing 22 different mineral samples for LIBS calibration, a diamond sample for Raman checking, 5 reflectance standards, an organic sample, a sample from Mars and imaging calibration targets.

The purpose of this work has been centered on the 22 mineral samples of the SCCT, checking the fulfillment of two requirements, the testing of major, minor and trace elements at the XRF scale and the characterization for heterogeneity.

The results of the homogeneity tests showed the elements that are homogeneously distributed over the whole surface of the SCCT samples. The major, minor and trace elements showing a homogeneous distribution are those with %RSD values in Tables 7 and 8 respectively. Those are suggested %RSD values as obtained from the weight average values from the different EDXRF and LIBS tests performed on the targets, and can be used to check the performance of SuperCam-LIBS spectrometer all along the mission.

Moreover, the Raman analysis on 9 of the 22 mineral samples revealed also which of the mineral phases showed a homogeneous distribution on the whole surface of the targets. For those 9 targets showing a Raman response, the most adequate wavenumbers have been selected to check the performance of the SuperCam-Raman device in Martian conditions.

For the homogeneously distributed elements and minerals, the different spectral features that SuperCam will obtain from the SCCT ensure its functionality for calibration checks on the FM model on Mars, or for calibration purposes on Earth (FS and EQM models), as well as for checking changes with time due to the hard environmental conditions or the influence of the dust as the mission goes on.

Declaration of competing interest

The authors declare that they have no known competing financial interests or personal relationships that could have appeared to influence the work reported in this paper.

CRediT authorship contribution statement

J.M. Madariaga: Conceptualization, Formal analysis, Funding acquisition, Project administration, Visualization, Writing – original draft, Writing – review & editing. **J. Aramendia:** Data curation, Investigation, Visualization, Writing – original draft, Writing – review & editing. **G. Arana:** Methodology, Validation, Writing – original draft, Writing – review & editing. **K. Castro:** Methodology, Validation, Writing – original draft, Writing – review & editing. **L. Gómez-Nubla:** Investigation, Writing – review & editing. **S. Fdez-Ortiz de Vallejuelo:** Investigation, Writing – review & editing. **C. Garcia-Florentino:** Investigation. **M. Maguregui:** Methodology, Writing – review & editing. **J.A. Manrique:** Data curation, Formal analysis, Investigation, Visualization, Writing – review & editing. **G. Lopez-Reyes:** Investigation, Writing – review & editing. **J. Moros:** Data curation, Writing – review & editing. **A. Cousin:** Data curation, Formal analysis, Investigation, Writing – original draft, Writing – review & editing. **S. Maurice:** Conceptualization, Funding acquisition, Project administration, Writing – original draft, Writing – review & editing. **A.M. Ollila:** Formal analysis, Investigation, Writing – review & editing. **R.C. Wiens:** Conceptualization, Funding acquisition, Project administration, Writing – original draft, Writing – review & editing. **F. Rull:** Conceptualization, Funding acquisition, Project administration, Validation. **J. Laserna:** Conceptualization, Funding acquisition, Project administration, Supervision, Validation, Writing – review & editing. **V. Garcia-Baonza:** Project administration, Writing – original draft, Writing – review & editing. **M. B. Madsen:** Validation, Writing – review & editing. **O. Forni:** Supervision, Validation, Writing – review & editing. **J. Lasue:** Conceptualization, Funding acquisition, Project administration, Supervision, Validation, Writing – review & editing. **S.M. Clegg:** Data curation, Writing – review & editing. **S. Robinson:** Supervision, Writing – review & editing. **P. Bernardi:** Supervision, Visualization, Writing – review & editing. **A.J. Brown:** Writing – review & editing. **P. Caïs:** Validation, Writing – review & editing. **J. Martinez-Frias:** Visualization, Writing – review & editing. **P. Beck:** Supervision, Visualization, Writing – review & editing. **S. Bernard:** Supervision, Writing – review & editing. **M.H. Bernt:** Supervision, Writing – review & editing. **O. Beyssac:** Methodology, Writing – original draft, Writing – review & editing. **E. Cloutis:** Writing – original draft, Methodology, Writing – review & editing. **C. Drouet:** Methodology, Writing – review & editing. **G. Dromart:** Methodology, Writing – review & editing. **B. Dubois:** Investigation, Writing – review & editing. **C. Fabre:** Writing – review & editing. **O. Gasnault:** Formal analysis, Writing – review & editing. **I. Gontijo:** Formal analysis, Writing – original draft, Writing – review & editing. **J.R. Johnson:** Methodology, Writing – review & editing. **J. Medina:** Data curation, Writing – review & editing. **P.-Y. Meslin:** Investigation, Writing – review & editing. **G. Montagnac:** Investigation, Writing – review & editing. **V. Sautter:** Methodology, Writing – review & editing. **S.K. Sharma:** Methodology, Writing – review & editing. **M. Veneranda:** Formal analysis, Investigation, Writing – review & editing. **P.A. Willis:** Formal analysis, Writing – review & editing.

Declaration of competing interest

The authors declare that they have no known competing financial interests or personal relationships that could have appeared to influence the work reported in this paper.

Acknowledgements

The authors would like to thank the Spanish Agency for Research, projects ESP2015-71965-REDT, ESP2017-87690-C3-1-R and RED2018-102600-T for funding as well as to local and regional institutions including the Basque Government, the University of the Basque Country, the Junta de Castilla y León, the University of Valladolid and the University of Malaga for their support. Support in the US was provided by NASA's Mars Exploration Program. Support in France was provided by CNES, CNRS, and local Universities. The Danish contribution was funded through support by the Carlsberg Foundation, grants CF16-0981 and CF17-0979. The team from the University of the Basque Country is very grateful to Sebastien Maussang and Victor Escobar from Renishaw for having faith in our work. The suggestions from T.R. Gabriel are gratefully acknowledged.

Appendix A. Supplementary data

Supplementary data to this article can be found online at https://doi.org/10.1016/j.aca.2022.339837.

References

[1] K.A. Farley, K.H. Williford, K.M. Stack, R. Bhartia, A. Chen, Manuel de la Torre, K. Hand, Y. Goreva, C.D.K. Herd, R. Hueso, Y. Liu, J.N. Maki, G. Martinez, R. C. Moeller, A. Nelessen, C.E. Newman, D. Nunes, A. Ponce, N. Spanovich, P. A. Willis, L.W. Beegle, J.F. Bell III, A.J. Brown, S.-E. Hamran, J.A. Hurowitz, S. Maurice, D.A. Paige, J.A. Rodriguez-Manfredi, M. Schulte, R.C. Wiens, Mars2020 mission overview, Space Sci. Rev. 216 (2020) 142, https://doi.org/10.1007/s11214-020-00762-y.

[2] A.R. Vasavada, J.P. Grotzinger, R.E. Arvidson, F.J. Calef, J.A. Crisp, S. Gupta, J. Hurowitz, N. Mangold, S. Maurice, M.E. Schmidt, R.C. Wiens, R.M.E. Williams, R.A. Yingst, Overview of the Mars science laboratory mission: Bradbury landing to Yellowknife Bay and beyond, J. Geophys. Res. Planets 119 (2014) 1134–1161, https://doi.org/10.1002/2014JE004622.

[3] R.C. Wiens, S. Maurice, S.H. Robinson, A.E. Nelson, Ph Cais, P. Bernardi, R. T. Newell, S. Clegg, ShK. Sharma, S. Storms, J. Deming, D. Beckman, A.M. Ollila, O. Gasnault, R.B. Anderson, Y. André, S.M. Angel, G. Arana, E. Auden, P. Beck, J. Becker, K. Benzerara, S. Bernard, O. Beyssac, L. Borges, B. Bousquet, K. Boyd, M. Caffrey, J. Carlson, K. Castro, J. Celis, B. Chide, K. Clark, E. Cloutis, E. C. Cordoba, A. Cousin, M. Dale, L. Deflores, D. Delapp, M.l Deleuze, M. Dirmyer, C. Donny, G. Dromart, M.G. Duran, M. Egan, J. Ervin, C. Fabre, A. Fau, W. Fischer, O. Forni, T. Fouchet, R. Fresquez, J. Frydenvang, D. Gasway, I. Gontijo, J. Grotzinger, X. Jacob, S. Jacquinod, J.R. Johnson, R.A. Klisiewicz, J. Lake, N. Lanza, J. Laserna, J. Lasue, S. Le Mouélic, C. Legett IV, R. Leveille, E. Lewin, G. Lopez-Reyes, R. Lorenz, E. Lorigny, S.P. Love, B. Lucero, J.M. Madariaga, M. Madsen, S. Madsen, N. Mangold, J.A. Manrique, J.P. Martinez, J. Martinez-Frias, K.P. McCabe, T.H. McConnochie, J.M. McGlown, S.M. McLennan, N. Melikechi, P.-Y. Meslin, J.M. Michel, D. Mimoun, A. Misra, G. Montagnac, F. Montmessin, V. Mousset, N. Murdoch, H. Newsom, L.A. Ott, Z.R. Ousnamer, L. Pares, Y. Parot, R. Pawluczyk, C.G. Peterson, P. Pilleri, P. Pinet, G. Pont, F. Poulet, C. Provost, B. Quertier, H. Quinn, W. Rapin, J.-M. Reess, A.H. Regan, A. L. Reyes-Newell, P.J. Romano, C. Royer, F. Rull, B. Sandoval, J.H. Sarrao, V. Sautter, M.J. Schoppers, S. Schröder, D. Seitz, T. Shepherd, P. Sobron, B. Dubois, V. Sridhar, M.J. Toplis, I. Torre-Fdez, I.A. Trettel, M. Underwood, A. Valdez, J. Valdez, D. Venhaus, P. Willis, The SuperCam instrument suite on the NASA Mars 2020 rover: body unit and combined system tests, Space Sci. Rev. 217 (2021) 4, https://doi.org/10.1007/s11214-020-00777-5.

[4] S. Maurice, R.C. Wiens, P. Bernardi, P. Caïs, S. Robinson, T. Nelson, O. Gasnault, J.-M. Reess, M. Deleuze, F. Rull, J.-A. Manrique, S. Abbaki, R.B. Anderson, Y. André, S.M. Angel, G. Arana, T. Battault, P. Beck, K. Benzerara, S. Bernard, J.-P. Berthias, O. Beyssac, M. Bonafous, B. Bousquet, M. Boutillier, A. Cadu, K. Castro, F. Chapron, B. Chide, K. Clark, S. Clegg, E. Cloutis, C. Collin, E.C. Cordoba, A. Cousin, J.-C. Dameury, W. D'Anna, Y. Daydou, L. Deflores, E. Dehouck, D. Delapp, G. De Los Santos, C. Donny, G. Dromart, B. Dubois, A. Dufour, M. Dupieux, M. Egan, J. Ervin, C. Fabre, A. Fau, W. Fischer, O. Forni, T. Fouchet, J. Frydenvang, S. Gauffre, M. Gauthier, V. Gharakanian, O. Gilard, I. Gontijo, R. Gonzalez, D. Granena, J. Grotzinger, R. Hassen-Khodja, M. Heim, Y. Hello, G. Hervet, O. Humeau, X. Jacob, S. Jacquinod, J.R. Johnson, D. Kouach, G. Lacombe, N. anza, L. Lapauw, J. Laserna, J. Lasue, L. Le Deit, S. Le Mouélic, E. Le Comte, Q.-M. Lee, C. Legett IV, R. Leveille, E. Lewin, G. Lopez-Reyes, R. Lorenz, B. Lucero, J.M. Madariaga, S. Madsen, M. Madsen, N. Mangold, F. Manni, J.-F. Mariscal, J. Martinez-Frias, K. Mathieu, R. Mathon, K.P. McCabe, T. McConnochie, S.M. McLennan, J. Mekki, N. Melikechi, P.-Y. Meslin, Y. Micheau, Y. Michel, J.M. Michel, D. Mimoun, A. Misra, G. Montagnac, C. Montaron, F. Montmessin, J. Moros, V. Mousset, Y. Morizet, N. Murdoch, R.T. Newell, H. Newsom, N.N. Tuong, A.M. Ollila, G. Orttner, L. Oudda, L. Pares, J. Parisot, Y. Parot, R. Pérez, D. Pheav, L. Picot, P. Pilleri, C. Pilorget, P. Pinet, G. Pont, F. Poulet, C. Quantin-Nataf, B. Quertier, D. Rambaud, W. Rapin, P. Romano, L. Roucayrol, C. Royer, M. Ruellan, B. F. Sandoval, V. Sautter, M.J. Schoppers, S. Schröder, H.-C. Seran, S.K. Sharma, P. Sobron, M. Sodki, A. Sournac, V. Sridhar, D. Standarovsky, S. Storms, N. Striebig, M. Tatat, M. Toplis, I. Torre-Fdez, N. Toulemont, C. Velasco, M. Veneranda, D. Venhaus, C. Virmontois, M. Viso, P. Willis, K.W. Wong, The SuperCam instrument suite on the Mars 2020 rover: science objectives and mast-unit description, Space Sci. Rev. 217 (2021) 47, https://doi.org/10.1007/s11214-021-00807-w.

[5] R.C. Wiens, S. Maurice, B. Barraclough, M. Saccoccio, W.C. Barkley, J.F. Bell III, S. Bender, J. Bernardin, D. Blaney, J. Blank, M. Bouyé, N. Bridges, N. Bultman, P. Caïs, R.C. Clanton, B. Clark, S. Clegg, A. Cousin, D. Cremers, A. Cros, L. DeFlores, D. Delapp, R. Dingler, C. D'Uston, M.D. Dyar, T. Elliott, D. Enemark, C. Fabre, M. Flores, O. Forni, O. Gasnault, T. Hale, C. Hays, K. Herkenhoff, E. Kan, L. Kirkland, D. Kouach, D. Landis, Y. Langevin, N. Lanza, F. LaRocca, J. Lasue, J. Latino, D. Limonadi, C. Lindensmith, C. Little, N. Mangold, G. Manhes, P. Mauchien, C. McKay, E. Miller, J. Mooney, R.V. Morris, L. Morrison, T. Nelson, H. Newsom, A. Ollila, M. Ott, L. Pares, R. Perez, F. Poitrasson, C. Provost, J. W. Reiter, T. Roberts, F. Romero, V. Sautter, S. Salazar, J.J. Simmonds, R. Stiglich, S. Storms, N. Striebig, J.-J. Thocaven, T. Trujillo, M. Ulibarri, D. Vaniman, N. Warner, R. Waterbury, R. Whitaker, J. Witt, B. Wong-Swanson, The ChemCam instruments on the Mars Science laboratory (MSL) rover: body unit and combined system performance, Space Sci. Rev. 170 (2012) 167–227, https://doi.org/10.1007/s11214-012-9902-4.

[6] S. Maurice, R.C. Wiens, M. Saccoccio, B. Barraclough, O. Gasnault, O. Forni, N. Mangold, D. Baratoux, S. Bender, G. Berger, J. Bernardin, M. Berthé, N. Bridges, D. Blaney, M. Bouyé, P. Caïs, B. Clark, S. Clegg, A. Cousin, D. Cremers, A. Cros, L. DeFlores, C. Derycke, B. Dingler, G. Dromart, B. Dubois, M. Dupieux, E. Durand, L. d'Uston, C. Fabre, B. Faure, A. Gaboriaud, T. Gharsa, K. Herkenhoff, E. Kan, L. Kirkland, D. Kouach, J.-L. Lacour, Y. Langevin, J. Lasue, S. Le Mouélic, M. Lescure, E. Lewin, D. Limonadi, G. Manhès, P. Mauchien, C. McKay, P.-Y. Meslin, Y. Michel, E. Miller, H.E. Newsom, G. Orttner, A. Paillet, L. Parès, Y. Parot, R. Pérez, P. Pinet, F. Poitrasson, B. Quertier, B. Sallé, C. Sotin, V. Sautter, H. Séran, J.J. Simmonds, J.-B. Sirven, R. Stiglich, N. Striebig, J.-J. Thocaven, M. J. Toplis, D. Vaniman, The ChemCam instruments on the Mars Science laboratory (MSL) rover: science objectives and mast unit, Space Sci. Rev. 170 (2012) 95–166, https://doi.org/10.1007/s11214-012-9912-2.

[7] J.A. Manrique, G. Lopez-Reyes, A. Cousin, F. Rull, S. Maurice, R.C. Wiens, M. B. Madsen, J.M. Madariaga, O. Gasnault, J. Aramendia, G. Arana, P. Beck, S. Bernard, P. Bernardi, M.H. Bernt, A. Berrocal, O. Beyssac, P. Caïs, C. Castro, K. Castro, S.M. Clegg, E. Cloutis, G. Dromart, C. Drouet, B. Dubois, D. Escribano, C. Fabre, A. Fernandez, O. Forni, V. Garcia-Baonza, I. Gontijo, J. Johnson, J. Laserna, J. Lasue, S. Madsen, E. Mateo-Marti, J. Medina, P.-Y. Meslin, G. Montagnac, A. Moral, J. Moros, A.M. Ollila, C. Ortega, O. Prieto-Ballesteros, J. M. Reess, S. Robinson, J. Rodriguez, J. Saiz, J.A. Sanz-Arranz, I. Sard, V. Sautter, P. Sobron, M. Toplis, M. Veneranda, SuperCam calibration targets: design and development, Space Sci. Rev. 216 (2020) 138, https://doi.org/10.1007/s11214-020-00764-w.

[8] R.C. Wiens, S. Maurice, J. Lasue, O. Forni, R.B. Anderson, S. Clegg, S. Bender, B. L. Barraclough, L. Deflores, D. Blaney, R. Perez, N. Lanza, A. Ollila, A. Cousin, O. Gasnault, D. Vaniman, M.D. Dyar, C. Fabre, V. Sautter, D. Delapp, H. Newsom, N. Melikechi and the ChemCam team, Pre-flight calibration and initial data processing for the ChemCam laser-induced breakdown spectroscopy instrument on the Mars Science Laboratory rover, Spectrochim. Acta B. 82 (2013) 1–27, https://doi.org/10.1016/j.sab.2013.02.003.

[9] A. Cousin, V. Sautter, C. Fabre, G. Dromart, G. Montagnac, C. Drouet, P.-Y. Meslin, O. Gasnault, O. Beyssac, S. Bernard, E. Cloutis, O. Forni, P. Beck, T. Fouchet, J. R. Johnson, J. Lasue, A.M. Ollila, P. De Parseval, S. Gouy, B. Caron, J. M. Madariaga, G. Arana, M. Bo Madsen, J. Laserna, J. Moros, J.A. Manrique, G. Lopez-Reyes, F. Rull, S. Maurice, R.C. Wiens, SuperCam calibration targets on board the perseverance rover: fabrication and quantitative characterization, Spectrochim. Acta, Part B 188 (2022), 106341, https://doi.org/10.1016/j.sab.2021.106341.

[10] S.L.R. Ellison, A. Williams, A. Eurachem, CITAC Guide CG4: Quantifying Uncertainty in Analytical Measurements, third ed., 2012. United Kingdom.

[11] A.M.H. van der Veen, T. Linsinger, J. Pauwels, Uncertainty calculations in the certification of reference materials. 2. Homogeneity study, Accred Qual. Assur. 6 (2001) 26–30, https://doi.org/10.1007/s007690000238.

[12] D. Fernandes Andrade, R. Cardoso Machado, E. Rodrigues Pereira-Filho, Proposition of electronic wastes as a reference material: part 2 – homogeneity, stability, characterization and uncertainties, J. Anal. At. Spectrom. 34 (1999) 2402–2410, https://doi.org/10.1039/C9JA00284G.

[13] G. Montagnac, G. Dromart, P. Beck, F. Mercier, B. Reynard, A. Cousin, S. Maurice, R. Wiens, Spark plasma sintering preparation of reference targets for field spectroscopy on Mars, J. Raman Spectrosc. 49 (2018) 1419–1425, https://doi.org/10.1002/jrs.5406.

[14] C. Fabre, S. Maurice, A. Cousin, R.C. Wiens, O. Forni, V. Sautter, D. Guillaume, Onboard calibration igneous targets for the Mars Science Laboratory Curiosity rover and the Chemistry Camera laser induced breakdown spectroscopy

instrument, Spectrochim. Acta B 66 (2011) 280–289, https://doi.org/10.1016/j.sab.2011.03.012.

[15] S. Bernard, O. Beyssac, K. Benzerara, Raman mapping using advanced line-scanning systems: geological applications, Appl. Spectrosc. 62 (2008) 1180–1188, https://doi.org/10.1366/000370208786401581.

[16] J. Aramendia, L. Gomez-Nubla, K. Castro, S. Fdez-Ortiz de Vallejuelo, G. Arana, M. Maguregui, V.G. Baonza, J. Medina, F. Rull, J.M. Madariaga, Overview of the techniques used for the study of non-terrestrial bodies: proposition of novel non-destructive methodology, Trends Anal. Chem. 98 (2018) 36–46, https://doi.org/10.1016/j.trac.2017.10.018.

[17] A.M. Ollila, H.E. Newsom, B. Clark III, R.C. Wiens, A. Cousin, J.G. Blank, N. Mangold, V. Sautter, S. Maurice, S.M. Clegg, et al., Trace element geochemistry (Li, Ba, Sr, and Rb) using Curiosity's ChemCam: early results for gale crater from Bradbury landing site to Rocknest, J. Geophys. Res. Planets 119 (2014) 255–285, https://doi.org/10.1002/2013JE004517.

[18] O. Forni, M. Gaft, M.J. Toplis, S.M. Clegg, S. Maurice, R.C. Wiens, N. Mangold, O. Gasnault, V. Sautter, S. Le Mouélic, et al., First detection of fluorine on Mars : implications for Gale crater's geochemistry, Geophys. Res. Lett. 42 (4) (2015) 1020–1028, https://doi.org/10.1002/2014GL062742.

[19] J. Lasue, S.M. Clegg, O. Forni, A. Cousin, R.C. Wiens, N. Lanza, N. Mangold, L. Le Deit, O. Gasnault, S. Maurice, et al., Observation of 5 wt% zinc by ChemCam libs at the Kimberley, gale crater, Mars, J. Geophys. Res. Planets 121 (2016) 338–352, https://doi.org/10.1002/2015JE004946.

[20] V. Payre, C. Fabre, A. Cousin, V. Sautter, R.C. Wiens, O. Forni, O. Gasnault, N. Mangold, P.Y. Meslin, J. Lasue, et al., Alkali trace elements in Gale crater, Mars, with ChemCam: calibration update and geological implications, J. Geophys. Res. Planets 122 (2017) 650–679, https://doi.org/10.1002/2016JE005201.

[21] P.Y. Meslin, J. Johnson, O. Forni, P. Beck, A. Cousin, J. Bridges, W. Rapin, B. Cohen, H.E. Newsom, V. Sautter, et al., Egg rock encounter: analysis of an iron-nickel meteorite found in gale crater by curiosity, 48th Lunar Planet, Sci. Conf. (2017) #2258.

[22] P.Y. Meslin, D. Wellington, R.C. Wiens, J. Johnson, J. Van Beek, O. Gasnault, V. Sautter, I. Maroger, J. Lasue, P. Beck, et al., Diversity and areal density of iron-nickel meteorites analyzed by ChemCam in Gale crater, 50th Lunar Planet, Sci. Conf. (2019) #3179.

[23] N.H. Thomas, B. Ehlmann, P.Y. Meslin, W. Rapin, D. Anderson, F. Rivera-Hernández, O. Forni, S. Schroeder, A. Cousin, N. Mangold, et al., Mars science laboratory observations of chloride salts in gale crater, Mars, Geophys. Res. Lett. 46 (2019) 10754–10763, https://doi.org/10.1029/2019GL082764.

[24] A. Wang, B. Jolliff, L. Haskin, K. Kuebler, K. Viskupic, Characterization and comparison of structural and compositional features of planetary quadrilateral pyroxenes by Raman spectroscopy, Am. Mineral. 86 (2001) 790–806, https://doi.org/10.2138/am-2001-0703.

[25] I. Torre-Fdez, J. Aramendia, L. Gomez-Nubla, K. Castro, J.M. Madariaga, Geochemical study of the Northwest Africa 6148 Martian meteorite and its terrestrial weathering processes, J. Raman Spectrosc. 48 (2017) 1536–1543, https://doi.org/10.1002/jrs.5148.

[26] I. Torre-Fdez, C. Garcia-Florentino, J. Huidobro, L. Coloma, P. Ruiz-Galende, J. Aramendia, K. Castro, G. Arana, J.M. Madariaga, Characterization of Olivines and their metallic composition: Raman Spectroscopy could provide an accurate solution for the active and future Mars missions, Eur. Planet. Sci. Conf. vol. 15 (2021) #586.